Meteorol. Atmos. Phys. 72, 185–202 (2000)

Meteorology
and Atmospheric
Physics

[1]Laboratoire d'Aérologie (CNRS-UPS), Toulouse, France
[2]National Center for Atmospheric Research* Boulder, Co, USA

Observation of Precipitating Systems over Complex Orography with Meteorological Doppler Radars: A Feasibility Study

J. F. Georgis[1], **F. Roux**[1], and **P. H. Hildebrand**[2]

With 5 Figures

Received March 22, 1999
Revised June 1, 1999

Summary

This paper concerns the use of airborne or ground-based Doppler radars to observe precipitating systems over complex orography. As nearly all of the previous experiments involving Doppler radars were conducted over flat surfaces over the continents or the oceans, new techniques are needed firstly to separate ground clutter from meteorological signal and, in the case of airborne Doppler observations, to deduce navigational errors. Secondly, it is necessary to take the atmospheric circulation induced by orography into account in the three-dimensional wind field analysis. Variational techniques are presented to solve these problems.

The proposed methods are tested with simulated ground-based and airborne Doppler radar observations for analytic flows over analytic terrains and for numerically simulated wind and reflectivity fields for the Brig event (22 September 1993) of heavy precipitation over the southern flank of the Alps (Cosma and Richard, 1998), and with actual airborne Doppler data relative to weak snow showers over the Rocky Mountains on 12 March 1995.

1. Introduction

A large variety of instruments are used to observe and describe the internal structure of clouds. But only Doppler radars can provide simultaneous information on the wind and precipitation fields with mesoscale coverage and convective-scale resolution. Since about twenty years, these instruments have contributed to better understand the kinematic, microphysical and even thermodynamic processes leading to the formation, maintenance and evolution of precipitating systems. Until now however, Doppler radars have been used mainly over oceans and flat terrains. To our knowledge, only two meteorological experiments over rugged terrains relied on dual- or multiple-Doppler radar observations and, consequently, were likely to provide information about the relationship between orography and three-dimensional wind field. These are the multiple-Doppler radar observations of cumulonimbus clouds over the Rocky Mountains by Cotton et al. (1983), and the investigation of precipitating clouds by airborne Doppler radar upstream of a mountain range near the Oregon coastline during the COAST campaign (Bond et al., 1997; Braun et al., 1997). But the first study focused only on the evolution of the reflectivity pattern, and the analysis of the radar-derived kinematic fields for the second one was hampered by large uncertainties in the velocity components, resulting probably from the approximations made for the calculation of the vertical wind.

The forthcoming Mesoscale Alpine Programme [MAP, Binder et al., 1995] will see a large deployment of airborne and ground-based

---

*The National Center for Atmospheric Research is sponsored by the United States' National Science Foundation.

Doppler radars over the Alps, so as to deduce the structure and evolution of the wind and reflectivity fields associated with orographic precipitating systems. Beforehand, it is necessary to verify that the difficulties encountered during previous studies are overcome and that reliable information will be deduced from radar observations. To this goal, new techniques have been developed which explicitely take the orographic effects into account.

A first aspect concerns a reliable identification of the ground clutter for two purposes. Firstly, such signals must be removed from the raw radar data, so as to retain only meteorological measurements. Secondly, comparisons between a radar-derived cartography of the ground and a digital terrain map (DTM) can be used to deduce information on possible position, navigation and/or attitude errors. Although this last aspect is more crucial for airborne radars, it may also be of some importance for ground-based ones.

The second aspect to deal with concerns the retrieval of balanced wind fields over complex terrains. It is well known that only the horizontal components of the wind can be directly determined from Doppler data with sufficient accuracy (see, e.g., Matejka and Barnes, 1998, for a review). The vertical component has to be deduced from the integration of the air mass continuity equation with adequate boundary conditions. But this calculation is not trivial because a direct upward integration leads inevitably to errors which amplify exponentially with height, whereas downward integration starting from a hypothetic tropopause level may lead to non-negligible biases. Only a variational approach permits to overcome these difficulties: Ray et al. (1980), Chong and Testud (1983) have shown that three-dimensional wind field can efficiently be calculated from multiple Doppler observations over a flat surface.

The calculation of the vertical component of the wind is far more difficult over complex orography, especially because of the influence of slope winds. Hence, the boundary conditions which must be specified before integrating the air mass continuity equation have to be carefully redefined. In particular, the vertical wind component at the ground level is no longer zero but, as a first approximation, is supposed equal to the product of the horizontal surface wind by the gradient of the terrain elevation. Additional classical constraints are added in the variational formulation, so as to minimize the vertical velocity at the top of the radar echoes and its horizontal gradient throughout the considered domain.

Section 2 concerns the objective identification of the ground clutter. Its use to deduce navigation errors is discussed in section 3. The details of the variational technique which permits to retrieve balanced three-dimensional wind fields over complex terrain are given in section 4. The results of tests with simulated data from analytical winds and orographies, and from numerical model outputs are discussed in section 5. Section 6 concerns an application to actual data collected during a test-flight over the Rocky Mountains in Colorado (USA) on 12 March 1995 with the French-American ELDORA-ASTRAIA (Electra Doppler radar – Analyse Stéréoscopique par un Radar à Impulsions Aéroporté, Hildebrand et al., 1994) airborne Doppler radar.

2. Identification of Surface Echoes

Useful information can be obtained from Doppler radar observations over complex orography only if surface echoes and meteorological signals are correctly identified and separated. As discussed in, e.g. Testud et al. (1995) or Delrieu et al. (1995), the contribution of surface echo in the return signal for the different radar range gates depends on three factors:

(i) the portion of the footprint (i.e. the projection of the beam – usually defined as the one-way 3-dB main lobe – over the earth surface) it intersects,
(ii) the orientation of the surface with respect to that of the radar beam,
(iii) the effective radar backscattering cross-section of the considered surface.

Over mountainous regions, because of strong dependence of the returned echo power on incident angle and terrain type, as well as soil, vegetation, humidity and wind on the ground, these three effects can be of similar importance and lead to large variations of the ground signal intensity. However, when the angle between the radar beam and the intersecting surface is close to prependicular, the power of the signal returned from the ground is generally higher than that from meteorological targets and can be unambiguously identified within a small number of range gates.

Here, the location of the surface echo within the series of range gates for a given radar beam direction is determined with two simultaneous criteria. The equivalent reflectivity value and its gradient between the considered gate and the previous one must both be above some thresholds. In the case of airborne radar observations discussed below, these thresholds, 40 dBZ for reflectivity and $100\,\mathrm{dBZ}\cdot\mathrm{km}^{-1}$ for its gradient, are multiplied by $|\sin\beta|^{0.7}$, where β is the elevation with respect to the horizontal, so as to account for the overall decrease of the intensity of the surface signal for non-vertical radar beams. Exponent 0.7 was determined empirically from available airborne Doppler data from previous experiments over oceanic regions in the tropics and the mid-latitudes. For radar beams at, e.g., 10° below the horizontal, the reflectivity and gradient thresholds are 12 dBZ and $29\,\mathrm{dBZ}\cdot\mathrm{km}^{-1}$, respectively. Such a smooth decrease of the surface signal is observed only when an airborne radar is operated over a flat surface. Over complex terrains, and lake, sea or ocean surfaces with high winds, swells and waves, relatively strong surface clutters can be observed even at grazing incidence. However, only the beams at more than 10° below the horizontal are considered, because surface signal cannot be unambiguously detected for near-grazing rays. Hence, the identification of surface echoes is possible only at horizontal distances less than $[(z_{AC} - h)/\tan 10°]$, where $(Z_{AC} - h)$ is the aircraft altitude above surface level at the considered point.

Once a point has been recognized as a ground echo, its cartesian coordinates and a weight proportional to the equivalent reflectivity value and gradient are stored. Afterwards, these points are interpolated toward a cartesian grid, taking their relative weight into account and using a Cressman (1959) filtering function. As an example, Fig. 1a and b shows a comparison between digital terrain and radar-derived maps, for a 15-min flight interval with the ELDORA-ASTRAIA radar aboard the NCAR Electra aircraft over the San Juan mountains near Denver, Colorado, on 12 March 1995 between 0335 and 0350 (all times are UTC). As it will be shown below, weak snow showers were observed at this time with the radar. As the aircraft was flying about 3 km above ground level, surface altitude can be retrieved with the technique described above only within an approximately 35-km wide band centered on the aircraft track. Good correlation is found between the topographic features revealed by the two terrain maps, showing that, wherever this is geometrically possible, the ground echo can be unambiguously identified. The mean and rms (root mean square) differences between the raw radar- and interpolated DTM-derived surface altitudes are +125 and 240 m, respectively. We show below that these values can be substantially reduced.

3. Correction for Navigation Errors

As outlined by Testud et al. (1995), correct navigation of airborne meteorological radar data with respect to the earth is essential to meet the scientific requirements concerning data location and velocity accuracy. For this purpose, they have developed a technique using the location and the Doppler velocity of the radar echo returned from the earth's surface to determine corrections of navigation errors resulting from either antenna mounting or Inertial Navigation System (INS) drift or bias. However, this method can only be applied for radar data collected over sea or flat land surface. Below, an improved version of this technique is described, with three major characteristics:

(i) the surface altitude $h(x, y)$ is no longer supposed to be constant;
(ii) a comparison between the flight level wind measurements and the Doppler velocity values at low elevation (less than ±5°) and close radial distance (less than 3 km) is also taken into account;
(iii) errors on aircraft location are also considered.

The problem is expressed as the minimization of a cost-function resulting from the normalized sum of three contributions J_1, J_2 and J_3, with respect to the unknown errors in aircraft or radar attitude (roll ΔR, heading ΔH, pitch ΔP), horizontal aircraft speed ΔV, aircraft location (eastward Δx, northward Δy, upward Δz), and radar ranging (Δd_f and Δd_a for the fore and aft radars, respectively, for ELDORA-ASTRAIA). J_1 is a cost-function quantifying the difference between the N_{SURF} radar-derived surface altitudes $z_{\mathrm{RAD}}(n)$ and those interpolated from the DTM at the same horizontal locations $h_{\mathrm{DTM}}[x_{\mathrm{RAD}}(n),y_{\mathrm{RAD}}(n)]$, after adding the variations of z_{RAD} and h_{DTM} due to navigation errors:

$$J_1 = \sum_{n=1}^{N_{\mathrm{SURF}}} p_{\mathrm{SURF}}(n) \left\{ \begin{array}{l} \left[\begin{array}{l} z_{\mathrm{RAD}}(n) + \left(\dfrac{\partial z_{\mathrm{RAD}}}{\partial R}\right)\Delta R + \left(\dfrac{\partial z_{\mathrm{RAD}}}{\partial P}(n)\right)\Delta P + \Delta z \\ +\delta_{fa}\left(\dfrac{\partial z_{\mathrm{RAD}}}{\partial d}(n)\right)\Delta d_f + (1-\delta_{fa})\left(\dfrac{\partial z_{\mathrm{RAD}}}{\partial d}(n)\right)\Delta d_a \end{array} \right] \\ - \left[\begin{array}{l} h_{\mathrm{DTM}}[x_{\mathrm{RAD}}(n), y_{\mathrm{RAD}}(n)] \\ + \left(\dfrac{\partial h_{\mathrm{DTM}}}{\partial x_{\mathrm{RAD}}}\right) \left\langle \begin{array}{l} \left(\dfrac{\partial x_{\mathrm{RAD}}}{\partial R}(n)\right)\Delta R + \left(\dfrac{\partial x_{\mathrm{RAD}}}{\partial P}(n)\right)\Delta P + \left(\dfrac{\partial x_{\mathrm{RAD}}}{\partial H}(n)\right)\Delta H \\ +\Delta X + \delta_{fa}\left(\dfrac{\partial x_{\mathrm{RAD}}}{\partial d}(n)\right)\Delta d_f + (1-\delta_{fa})\left(\dfrac{\partial x_{\mathrm{RAD}}}{\partial d}(n)\right)\Delta d_a \end{array} \right\rangle \\ + \left(\dfrac{\partial h_{\mathrm{DTM}}}{\partial x_{\mathrm{RAD}}}\right) \left\langle \begin{array}{l} \left(\dfrac{\partial y_{\mathrm{RAD}}}{\partial R}(n)\right)\Delta R + \left(\dfrac{\partial y_{\mathrm{RAD}}}{\partial P}(n)\right)\Delta P + \left(\dfrac{\partial y_{\mathrm{RAD}}}{\partial H}(n)\right)\Delta H \\ +\Delta Y + \delta_{fa}\left(\dfrac{\partial y_{\mathrm{RAD}}}{\partial d}(n)\right)\Delta d_f + (1-\delta_{fa})\left(\dfrac{\partial y_{\mathrm{RAD}}}{\partial d}(n)\right)\Delta d_a \end{array} \right\rangle \end{array} \right] \end{array} \right\}^2 \quad (1)$$

surface reflectivity and gradient. The second cost-function J_2 deals with the N_{SURF} Doppler velocity values V_{SURF} associated with the surface echoes, which should be equal to zero if there was no error. Likewise, J_2 includes variations due to the aircraft attitude and horizontal speed errors:

$$J_2 = \sum_{n=1}^{N_{\mathrm{SURF}}} p_{\mathrm{SURF}}(n) \left\{ \left[\begin{array}{r} V_{\mathrm{SURF}}(n) + \left(\dfrac{\partial V_{\mathrm{SURF}}}{\partial R}(n)\right)\Delta R + \left(\dfrac{\partial V_{\mathrm{SURF}}}{\partial P}(n)\right)\Delta P \\ + \left(\dfrac{\partial V_{\mathrm{SURF}}}{\partial D}(n)\right)\Delta H + \left(\dfrac{\partial V_{\mathrm{SURF}}}{\partial V}(n)\right)\Delta V \end{array} \right] \right\}^2 \quad (2)$$

where the values of the partial derivatives of x_{RAD}, y_{RAD} and z_{RAD} with respect to aircraft roll, pitch, drift and radar range for each point (n) are obtained from simple geometry (see Appendix), δ_{fa} is equal to 1 (0) for the fore (aft) radar beams, p_{SURF} is a weight proportional to the where the values of the partial derivatives of V_{SURF} with respect to aircraft roll, pitch, drift and horizontal speed for each point (n) are deduced from geometry (App. A). The third cost-function J_3 concerns the N_{NEAR} differences between the Doppler velocity values V_{NEAR} at low elevation

(<±5°) and close horizontal distance (<3 km) from the aircraft, and the projection V_{INSITU} of the in-situ wind components on the direction toward which the radar beam is pointing, after adding the variations due to the aircraft attitude and speed errors:

$$J_3 = \sum_{n=1}^{N_{\mathrm{NEAR}}} p_{\mathrm{NEAR}}(n) \left\{ \begin{array}{c} \left[\begin{array}{c} V_{\mathrm{NEAR}}(n) + \left(\dfrac{\partial V_{\mathrm{NEAR}}}{\partial R}(n)\right)\Delta R + \left(\dfrac{\partial V_{\mathrm{NEAR}}}{\partial P}(n)\right)\Delta P \\ + \left(\dfrac{\partial V_{\mathrm{NEAR}}}{\partial H}(n)\right)\Delta H + \left(\dfrac{\partial V_{\mathrm{NEAR}}}{\partial V}(n)\right)\Delta V \end{array} \right] \\ - \left[\begin{array}{c} V_{\mathrm{INSITU}}(n) + \left(\dfrac{\partial V_{\mathrm{INSITU}}}{\partial R}(n)\right)\Delta R + \left(\dfrac{\partial V_{\mathrm{INSITU}}}{\partial P}(n)\right)\Delta P \\ + \left(\dfrac{\partial V_{\mathrm{INSITU}}}{\partial H}(n)\right)\Delta H + \left(\dfrac{\partial V_{\mathrm{INSITU}}}{\partial V}(n)\right)\Delta V \end{array} \right] \end{array} \right\}^2 \tag{3}$$

where $p_{\mathrm{NEAR}}(n)$ is a weight inversely proportional to the distance between the considered point and the aircraft. A solution for the navigational corrections is obtained through the minimization of the normalized sum J of J_1, J_2, J_3:

$$\begin{aligned} J = {} & \frac{J_1}{\sum_{n=1}^{N_{\mathrm{SURF}}} p_{\mathrm{SURF}}(n) \| z_{\mathrm{RAD}}(n) - h_{\mathrm{DTM}}[x_{\mathrm{RAD}}(n), y_{\mathrm{RAD}}(n)] \|} \\ & + \frac{J_2}{\sum_{n=1}^{N_{\mathrm{SURF}}} p_{\mathrm{SURF}}(n) \| V_{\mathrm{SURF}}(n) \|} \\ & + \frac{J_3}{\sum_{n=1}^{N_{\mathrm{NEAR}}} p_{\mathrm{NEAR}}(n) \| V_{\mathrm{NEAR}}(n) - V_{\mathrm{INSITU}}(n) \|} \end{aligned} \tag{4a}$$

where symbol $\|\|$ indicates a positive value. J is minimized with respect to the errors in roll, pitch, heading, aircraft horizontal position and altitude, radar range delays and horizontal groundspeed, as:

$$\frac{\partial J}{\partial(\Delta R, \Delta P, \Delta H, \Delta x, \Delta y, \Delta z, \Delta d_f, \Delta d_a, \Delta V)} = 0 \tag{4b}$$

Such a derivation gives a system of 9 linear equations, which can easily be solved through the inversion of a 9 × 9 matrix.

Though written differently, this formulation is equivalent to that used by Testud et al. (1995) when h_{DTM} is constant so its derivatives with respect to x_{RAD} and y_{RAD} cancel, and J_3, Δx and Δy are not considered in (4a and b). It can be noted that it is only for a rolling orography that errors $(\Delta x, \Delta y)$ on the horizontal position of the aircraft can be deduced and error ΔH on the heading angle H has an influence on the difference between the radar- and DTM-derived surface altitudes since, otherwise, terms $(\partial h_{\mathrm{DTM}}/\partial x_{\mathrm{RAD}})$ and $(\partial h_{\mathrm{DTM}}/\partial y_{\mathrm{RAD}})$ in (1) cancel (see Appendix).

A series of tests (not shown) with simulated data and orographies with added realistic errors (less than ±2° for the angles, less than ±1 km for aircraft horizontal location, less than ±500 m for aircraft altitude and range delay, less than $\pm 3\,\mathrm{ms}^{-1}$ for aircraft horizontal speed) and gaussian white noises on surface identification (100 m rms) and Doppler velocities ($2\,\mathrm{ms}^{-1}$ rms) has revealed that this method allows to deduce errors on angles, altitude and range delay, horizontal speed to within about 0.2°, 20 m and $0.5\,\mathrm{ms}^{-1}$, respectively. These values are slightly larger than those obtained by Testud et al. (1995) (0.1°, 10 m, $0.1\,\mathrm{ms}^{-1}$, as deduced from their Table 3), probably because of the more difficult identification of the surface over complex orography. It is also to be mentioned that, when errors Δx and Δy in aircraft location are large (>1 km) and the surface altitude is highly variable, the linearization of h_{DTM} with constant gradients $\partial h_{\mathrm{DTM}}/\partial x_{\mathrm{RAD}}$ and $\partial h_{\mathrm{DTM}}/\partial y_{\mathrm{RAD}}$ in (1) may not be accurate. In this case, an iterative series of less than five analyses (4a and b) can help to find Δx and Δy to within about 100 m. After the obtained corrections are applied to the simulated data, the mean and rms differences for surface altitude, surface Doppler velocity and

Doppler velocity at low elevation and close range reduce significantly. However it must be outlined that, although this method can help to significantly reduce biases resulting from navigation errors, it cannot make the random error or independent instrumental bias vanish.

Concerning the previously discussed ELDORA-ASTRAIA data set at 0335–0350 on 12 March 1995, the obtained corrections are −0.15° for roll, −1.45° for pitch, +0.20° for drift, +90 m and +75 m for the range delays of the fore and aft radars, +950 m for aircraft zonal position, −600 m for its meridional position, −55 m for aircraft altitude, $-1.1\,\mathrm{ms}^{-1}$ for horizontal aircraft speed, respectively. Using these corrections, the mean and rms differences for surface altitude at 0335–0350 reduce from +125 and 240 m to <1 and 170 m, respectively; those on surface Doppler velocity from +3.0 and $3.4\,\mathrm{ms}^{-1}$ to +0.2 and $1.1\,\mathrm{ms}^{-1}$; those on Doppler velocity at low elevation and close range from −0.4 and $5.6\,\mathrm{ms}^{-1}$ to −0.2 and $5.3\,\mathrm{ms}^{-1}$. This relatively small reduction of the rms difference for this last quantity, as compared to the surface Doppler velocity, could result from the largest retrieved error in the pitch angle ($\Delta P = -1.45^\circ$), which has a very small influence on the horizontal wind component, while the error in the more influential drift angle is relatively small $\Delta H = +0.20^\circ$) since, as it can be deduced from the Appendix, $\|\partial V_{\mathrm{INSITU}}/\partial P\|$ is significantly smaller than $\|\partial V_{\mathrm{INSITU}}/\partial H\|$. Since the mean difference between the Doppler and flight-level winds is however small, this could also reveal uncorrelated random variations for both measurements. The radar-derived surface terrain map obtained after these corrections have been applied (Fig. 1c) compares significantly better than the uncorrected map (Fig. 1b) with the DTM-derived one (Fig. 1a).

4. Retrieval of Balanced Three-Dimensional Wind Fields over Complex Orography

To isolate meteorological data from ground-based or airborne Doppler radar observations

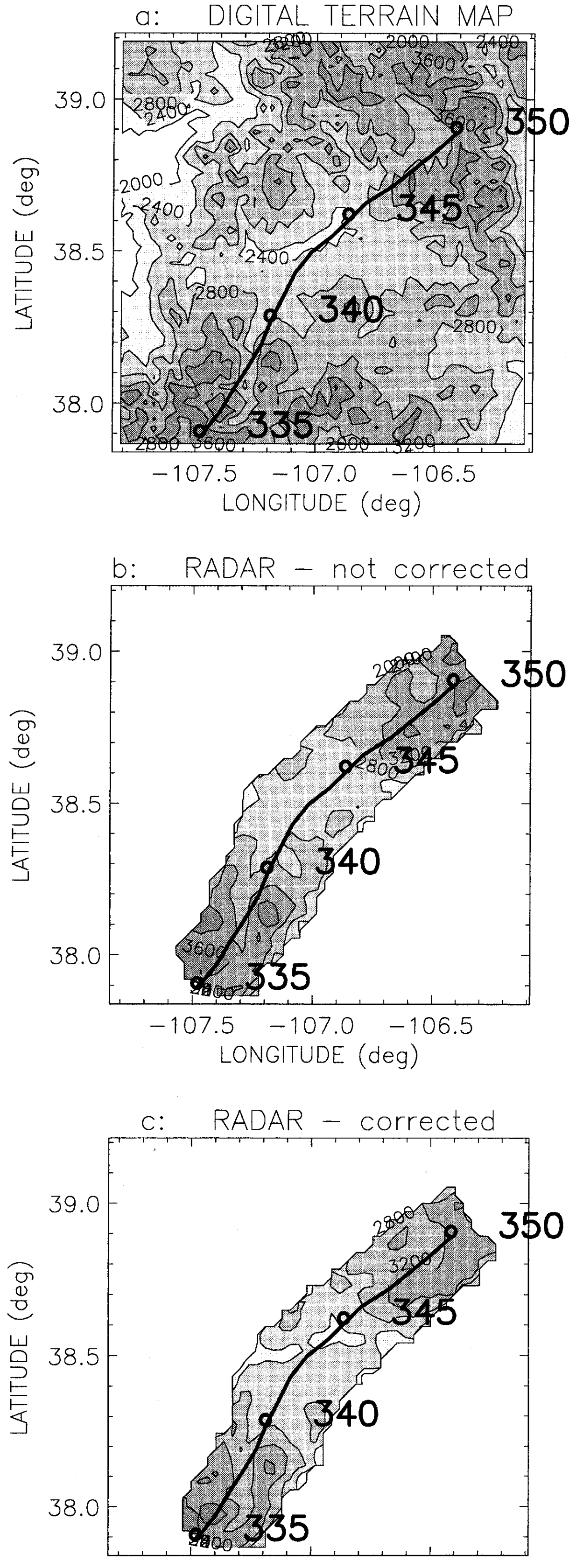

Fig. 1. Electra trajectory (solid line) and terrain elevation map (in m, starting from 2100 m, contours every 300 m) for the derived from (a) a digital terrain map, (b) uncorrected ELDORA-ASTRAIA radar data, (c) radar data corrected for navigational errors

over complex orography, the surface echoes are eliminated using both the objective identification technique described in Section 2 and the DTM in such a way that any range gate that could be even partially contaminated by surface echo, and those beyond, are eliminated. Then, different methods can be used to calculate three-dimensional wind fields from the Doppler velocities (see Matejka and Bartels, 1998, for a review). Two steps are considered here:

(i) horizontal wind components are calculated at grid points of a three-dimensional cartesian domain,

(ii) then the anelastic airmass continuity equation is integrated upwards while a minimum correction is applied to the three-dimensional wind so as to satisfy lower and upper boundary conditions as well as regularity of the vertical velocity field throughout the considered domain.

4.1 The Horizontal Wind Components

The radial velocity V measured with a ground-based or an airborne meteorological Doppler radar is the projection of the sum of the downward precipitation fallspeed V_P (positive downwards) relative to the air and the three-dimensional air speed onto the direction toward which the radar is pointing, as:

$$\begin{aligned}V = &-u\cos\alpha\cos\beta - v\sin\alpha\cos\beta\\ &-(w - V_P)\sin\beta\end{aligned} \tag{5}$$

where α and β are the azimuth with respect to east (north is 90°, west 180°, ...) and the elevation with respect to the horizontal (zenith is +90°, nadir is −90°), respectively; u, v and w the cartesian wind components, positive eastwards, northwards and upwards, respectively. The fallspeed V_P is estimated from the radar reflectivity values. Concerning the ELDORA-ASTRAIA data on 12 March 1995, we used the same relation as that for iced hydrometeors in Roux et al. (1993). As a first approximation, only the Doppler velocity data with $|\beta| < 30°$ are considered, so the contribution of the unknown vertical velocity component w in (5) can be neglected (but, in an iterative process, it can also be deduced from a previous analysis as $\tilde{w}$, see Section 4b). A « corrected » Doppler velocity V^* is obtained as:

$$\begin{aligned}V^* &= V - V_P\sin\beta(+\tilde{w}\sin\beta)\\ &\approx -u\cos\alpha\cos\beta - v\sin\alpha\cos\beta\end{aligned} \tag{6}$$

Following Roux and Sun (1990), the horizontal velocity components u_{ijk} and v_{ijk} are obtained at each grid point $[ijk]$ of a cartesian domain defined by $[x_i = x_0 + (i-1)\times\Delta_x$ for $1 \le i \le N_x$; $y_j = y_0 + (j-1)\times\Delta_Y$ for $1 \le j \le N_Y$; $Z_k = Z_0 + (k-1)\times\Delta_Z$ and $1 \le k \le N_Z]$, through the minimization of a series of $N_X \times N_Y \times N_Z$ cost-functions $J_{uv}(ijk)$ defined as:

$$J_{uv}(ijk) = \sum_{n=1}^{N_{ijk}} p_n(V_n^* + u_{ijk}\cos\alpha_n\cos\beta_n + v_{ijk}\sin\alpha_n\cos\beta_n)^2 \tag{7a}$$

$$\begin{aligned}\text{with}\quad & p_n = (3 - D_n^2/(3 + D_n^2) \quad \text{if}\quad D_n^2 = \frac{(x_n - x_i)^2}{\Delta_x^2} + \frac{(y_n - y_j)^2}{\Delta_Y^2} + \frac{(z_n - z_k)^2}{\Delta_Z^2} < 3\\ & p_n = 0 \qquad\qquad\qquad\quad \text{if}\quad D_n^2 \ge 3\end{aligned}$$

where x_n, y_n, z_n are the cartesian coordinates of the n$^{\text{th}}$ observed point in the vicinity of grid point x_i, y_j, z_k. Provided that there are enough measurements with different azimuths α_n (the standard deviation of the α's must be larger than 30°), the wind components u_{ijk} and v_{ijk} are obtained through:

$$\frac{\partial J_{uv}(ijk)}{\partial u_{ijk}} = 0 \quad\text{and}\quad \frac{\partial J_{uv}(ijk)}{\partial v_{ijk}} = 0 \tag{7b}$$

which can easily be solved through the inversion of a 2×2 matrix for each $[ijk]$ where the conditions above are satisfied. These values u_{ijk}

and v_{ijk} at each grid point are then checked for consistency with their neighbours, i.e. they are forced to be within the limits:

$$\begin{aligned} \langle u\rangle - \sigma_u \leq u_{ijk} \leq \langle u\rangle + \sigma_u \\ \langle v\rangle - \sigma_v \leq v_{ijk} \leq \langle v\rangle + \sigma_v \end{aligned} \tag{8}$$

where symbols $\langle\ \rangle$ and σ denote mean value and standard deviation for the ≤ 26 grid points at $[i \pm 1, j \pm 1, k \pm 1]$, excluding $[ijk]$.

4.2 The Vertical Wind Component

The radar-derived wind field is supposed to obey the anelastic approximation of the air mass continuity equation:

$$\frac{\partial u}{\partial x} + \frac{\partial v}{\partial y} + \frac{\partial w}{\partial z} - \frac{w}{H_0} = 0 \tag{9}$$

where H_0 is the density scale height, determined by $\rho(z) = \rho_0 \times \exp(z/H_0)$, where $\rho(z)$ and ρ_0 are the air density at altitude z and mean sea level, respectively. The vertical velocity component w_{ijk} can be deduced as:

$$\begin{aligned} w_{ijk} = {} & -\exp\left(\frac{z_k}{H_0}\right) \\ & \times \int_{h(x_i,y_j)}^{z_k} \exp\left(-\frac{\zeta_\kappa}{H_0}\right)\left(\frac{\partial u_{ijk}}{\partial x} + \frac{\partial v_{ij\kappa}}{\partial y}\right) d\zeta_\kappa \\ & + \exp\left[\frac{z - h(x_i, y_i)}{H_0}\right] w_{\mathrm{SURF}}(ij) \end{aligned} \tag{10}$$

where $h(x_i, y_j)$ is the surface altitude derived from a DTM and $w_{\mathrm{SURF}}(ij)$ is the vertical component of the wind at surface level below the considered grid point (ij). The latter contribution, which is zero in the case of a flat earth's surface, can be very important over steep terrain. As no information is generally available, we will suppose that w_{surf} results only from the flow following the terrain $h(x, y)$, as:

$$\begin{aligned} w_{\mathrm{SURF}}(ij) = {} & u[ij, h(x_i, y_j)]\,\frac{\partial h(x_i, y_j)}{\partial x} \\ & + v[ij, h(x_i, y_j)]\,\frac{\partial h(x_i, y_J)}{\partial y} \end{aligned} \tag{11}$$

with

$$\begin{aligned} u[ij, h(x_i, y_j)] = {} & u[ij, k_{\min}(ij)] \\ & + [h(x_i, y_j) - z_{\min}(ij)]\left\langle \frac{\partial u}{\partial z}\right\rangle_{k_{\min}} \end{aligned}$$

and (12)

$$\begin{aligned} v[ij, h(x_i, y_j)] = {} & v[ij, k_{\min}(ij)] \\ & + [h(x_i, y_j) - z_{\min}(ij)]\left\langle \frac{\partial v}{\partial z}\right\rangle_{k_{\min}} \end{aligned}$$

where $u[x_i, y_j, h(x_i, y_j)]$ and $v[x_i, y_j, h(x_i, y_j)]$ are the horizontal wind components at surface, extrapolated from the values at the lowest level $k_{\min}(ij)$ or altitude $z_{\min}(ij)$ where horizontal wind components are available, and the components $\langle \partial u/\partial z\rangle k_{\min}$ and $\langle \partial v/\partial z\rangle k_{\min}$ of the mean vertical wind shear determined from the wind components at the first three levels.

It is well known that calculation of the vertical velocity component through (10) is unstable with respect to errors in the horizontal wind component and divergence, which can lead to quite unrealistic values aloft (e.g., Matejka and Bartels, 1998). In order to correct for this effect and to insure mass balance within the considered domain, a method derived from that used by Roux and Viltard (1995) to analyze airborne Doppler data collected within Hurricane Claudette (1991) has been developed. The horizontal wind components are corrected by adding a term, constant with altitude, which derives from a scalar velocity potential $\phi(ij)$, as:

$$\begin{aligned} u^*(ijk) = u(ijk) + \frac{\partial \phi(ij)}{\partial x} \quad \text{and} \\ v^*(ijk) = v(ijk) + \frac{\partial \phi(ij)}{\partial y} \end{aligned} \tag{13}$$

Such a constant correction for each column $[ij, k = 1, N_Z]$ is minimum and insures that only the divergent part of the horizontal wind field is modified while its rotational part remains unchanged (Bijlsma et al., 1986). The corrected vertical wind component w^* is given by:

$$\begin{aligned} w^*(ijk) = {} & w(ijk) + A(ijk)\,\frac{\partial \phi(ij)}{\partial x} \\ & + B(ijk)\,\frac{\partial \phi(ij)}{\partial y} \\ & + C(ijk)\left[\frac{\partial^2 \phi(ij)}{\partial x^2} + \frac{\partial^2 \phi(ij)}{\partial y^2}\right] \end{aligned} \tag{14}$$

with:

$$
\begin{aligned}
A(ijk) &= \exp\left[\frac{z_k - h(x_i, y_j)}{H_0}\right]\frac{\partial h(x_i, y_j)}{\partial x},\\
B(ijk) &= \exp\left[\frac{z_k - h(x_i, y_j)}{H_0}\right]\frac{\partial h(x_i, y_j)}{\partial y}\\
c(ijk) &= -\exp\left(\frac{z_k}{H_0}\right)\int_{h(x_i,y_j)}^{z_k}\exp\left(-\frac{\zeta}{H_0}\right)d\zeta\\
&= H_0\left\{1 - \exp\left[\frac{z_k - h(x_i, y_j)}{H_0}\right]\right\}
\end{aligned}
\tag{15}
$$

Corrections $\phi(ij)$ are determined through minimization of cost-function J_ϕ, the normalized sum of mean vertical velocity at the upper boundary of the considered domain [part (a) of (16)] and mean horizontal gradient of vertical velocity within the domain [part (b)]:

$$
J_\phi = \underbrace{\frac{\sum_{ij}^{N_{\mathrm{TOP}}}\left\{\lambda(ijk_{\mathrm{TOP}})[w^*(ijk_{\mathrm{TOP}})]^2\right\}}{\sum_{ij}^{N_{\mathrm{TOP}}}\|\lambda(ijk_{\mathrm{TOP}})w(ijk_{\mathrm{TOP}})\|}}_{a}
+ \underbrace{\frac{\sum_{ijk}^{N_D}\left\{\left[\frac{\partial x^*(ijk)}{\partial x}\right]^2 + \left[\frac{\partial w^*(ijk)}{\partial y}\right]^2\right\}}{\sum_{ijk}^{N_D}\left[\left\|\frac{\partial w(ijk)}{\partial x}\right\| + \left\|\frac{\partial w(ijk)}{\partial y}\right\|\right]}}_{b}
\tag{16}
$$

where N_D is the number of radar-derived wind components within the three-dimensional domain, N_{TOP} the number of points on its upper surface $k_{\mathrm{TOP}}(ij)$. So as to take possible uncomplete radar sampling aloft into account, con-

$$
\begin{aligned}
J_\phi = {} & \frac{1}{\sum_{ij}^{N_{\mathrm{TOP}}}\|\lambda(ijk_{\mathrm{TOP}})W(ijk_{\mathrm{TOP}})\|}\sum_{ij}^{N_{\mathrm{TOP}}}\left\{\lambda_(ijk_{\mathrm{TOP}})\left[\begin{aligned}&W(ijk_{\mathrm{TOP}})\\ &\quad + A(ijk_{\mathrm{TOP}})\frac{\partial\phi(ij)}{\partial x} + B(ijk_{\mathrm{TOP}})\frac{\partial\phi(ij)}{\partial y}\\ &\quad + C(ijk_{\mathrm{TOP}})\left[\frac{\partial^2\phi(ij)}{\partial x^2} + \frac{\partial^2\phi(ij)}{\partial y^2}\right]\end{aligned}\right]\right\}^2\\
& + \frac{1}{\sum_{ijk}^{N_D}\left[\left\|\frac{\partial w(ijk)}{\partial x}\right\| + \left\|\frac{\partial w(ijk)}{\partial y}\right\|\right]}\sum_{ijk}^{N_D}\left\{\begin{aligned}&\left[\begin{aligned}&\frac{\partial w}{\partial x}(ijk) + A(ijk)\frac{\partial^2\phi(ij)}{\partial x^2} + \frac{\partial A(ijk)}{\partial x}\frac{\partial\phi(ij)}{\partial x}\\ &\quad +B(ijk)\frac{\partial^2\phi(ij)}{\partial x\partial y} + \frac{\partial B(ijk)}{\partial x}\frac{\partial\phi(ij)}{\partial y}\\ &\quad +C(ijk)\left[\frac{\partial^3\phi(ij)}{\partial x^3} + \frac{\partial^3\phi(ij)}{\partial x\partial y^2}\right]\\ &\quad +\frac{\partial C(ijk)}{\partial x}\left[\frac{\partial^2\phi(ij)}{\partial x^2} + \frac{\partial^2\phi(ij)}{\partial y^2}\right]\end{aligned}\right]^2\\ &+\left[\begin{aligned}&\frac{\partial W}{\partial y}(ijk) + A(ijk)\frac{\partial^2\phi(ij)}{\partial x\partial y} + \frac{\partial A(ijk)}{\partial y}\frac{\partial\phi(ij)}{\partial x}\\ &\quad +B(ijk)\frac{\partial^2\phi(ij)}{\partial y^2} + \frac{\partial B(ijk)}{\partial y}\frac{\partial\phi(ij)}{\partial y}\\ &\quad +C(ijk)\left[\frac{\partial^3\phi(ij)}{\partial x^2\partial y} + \frac{\partial^3\phi(ij)}{\partial y^3}\right]\\ &\quad +\frac{\partial C(ijk)}{\partial y}\left[\frac{\partial^2\phi(ij)}{\partial x^2} + \frac{\partial^2\phi(ij)}{\partial y^2}\right]\end{aligned}\right]^2\end{aligned}\right\}
\end{aligned}
\tag{17a}
$$

straint (a) is more (resp. less) stricty applied when the observed radar reflectivity is relatively low (resp. high): $\lambda(ijk_{\mathrm{TOP}})$ is set to 1 when radar reflectivity $\eta(ijk_{\mathrm{TOP}})$ is 0 dBZ or less, to 0.5 for the maximum of the reflectivity values on the upper surface $k_{\mathrm{TOP}}(ij)$, with a smooth interpolation between these two limits.

Expressing (16) in terms of $\phi(ij)$ gives Eq. 17a (see previous page).

Note that J_ϕ becomes much simpler when the earth's surface above which radar observations are collected is flat [i.e. $h(x,y) = h_0$ in (15)], since terms A and B vanish, and C is then a function of altitude z only. In any case, a solution for $\phi(ij)$ is obtained through the minimization of J_ϕ as:

$$\frac{\partial J_\phi}{\partial \phi(ij)} = 0 \text{ for } 1 \leq i \leq N_x \quad \text{and} \quad 1 \leq j \leq N_Y \tag{17b}$$

After linearization of (17a) using finite differences, (17b) is equivalent to a set of $N_X \times N_Y$ linear equations with $N_X \times N_Y$ unknowns $\phi(ij)$, which are solved with the Conjugate Gradient algorithm (Hestenes and Stiefel, 1952). The obtained $\phi(ij)$ are used to correct the horizontal wind components through (13) and the vertical one through (14), which provides a three-dimensional wind field strictly obeying the continuity equation (9) and verifying the constraints expressed in (16). In an iterative analysis, the obtained vertical velocity values are interpolated to correct for their contribution in the input Doppler velocities in (6). The whole calculation of the horizontal, then vertical wind components is iterated until the rms difference between two successive vertical velocity fields becomes negligible (e.g., less than 0.01 ms^{-1}).

5. Application to Simulated Data

This method has been firstly validated with a series of tests using analytically simulated orographies (e.g., Fig. 2a) and wind fields (e.g., Fig. 2b and c), so that the air velocity is parallel to the terrain at surface level and vertical velocity vanishes at 10 km altitude (pseudo-tropopause level). To simulate radar error, a gaussian white noise of 2 ms^{-1} rms value was added to each of the horizontal wind component. The velocity values retrieved from (13) and (14) (where u and v stand for the «noisy» input values) after the minimization of (17) are compared to the noise-free analytical wind. The vertical velocity contours at 6 km altitude (Fig. 2d) and the vertical cross-section at Y = 38.2 km (Fig. 2e) display features very similar to, though slightly smoother than those shown in Fig. 2b and c, respectively.

An important aspect of this method is that, owing to the global minimization, it tolerates missing data in the low levels, a situation that frequently occurs with radar observations over mountainous regions. As an example, Fig. 2f and g show the same vertical velocity contours and vertical cross-section as those in Fig. 2d and e, except the input horizontal velocity values within [11<X<38 km, 23<Y<46 km, Z<3.2 km] (dashed line contour in Fig. 2f, 61% of the input data below 3.2 km altitude) are not taken into account. Although slightly weaker vertical velocities are deduced in this region, the retrieved features are again very similar to the «actual» ones in Fig. 2b and c.

More specifically, Table 1 summarizes the characteristics of the analyzed wind fields. As seen in Table 1, the rms values of horizontal wind and added correction $[\langle(\partial\phi/\partial x)^2 + (\partial\phi/\partial y)^2\rangle^{1/2} = \langle(\Delta u)^2 + (\Delta v)^2\rangle^{1/2}$, see (13)] are 7.99 and 1.93 ms^{-1}, respectively, when all the input data are taken into account. The rms values of horizontal divergence and added correction $[\langle(\partial^2\phi/\partial x^2 + \partial^2\phi/\partial y^2)^2\rangle^{1/2}] = \langle\Delta(\partial u/\partial x + \partial v/\partial y)^2\rangle^{1/2}$ are 1.06 and 0.19×10^{-3} s^{-1}, respectively. The rms values of vertical velocity at echo top (10 km altitude in Fig. 2) and of its horizontal gradient throughout the domain decrease from 3.25 to 0.10 ms^{-1}, and from 2.04 to 0.44×10^{-3} s^{-1}, respectively. Standard deviations between the retrieved and «actual» horizontal and vertical winds are 1.11 and 0.45 ms^{-1}, respectively. Very similar values are obtained when low-level data are not taken into account, with however slightly larger standard deviations (1.15 and 0.52 ms^{-1} for the horizontal and vertical winds, respectively). It is to be outlined that the slightly smaller horizontal gradients of vertical velocity (0.44 and 0.43×10^{-3} s^{-1}), as compared to the «actual» value of 0.53×10^{-3} s^{-1}, reveal some inherent smoothing, as it was also

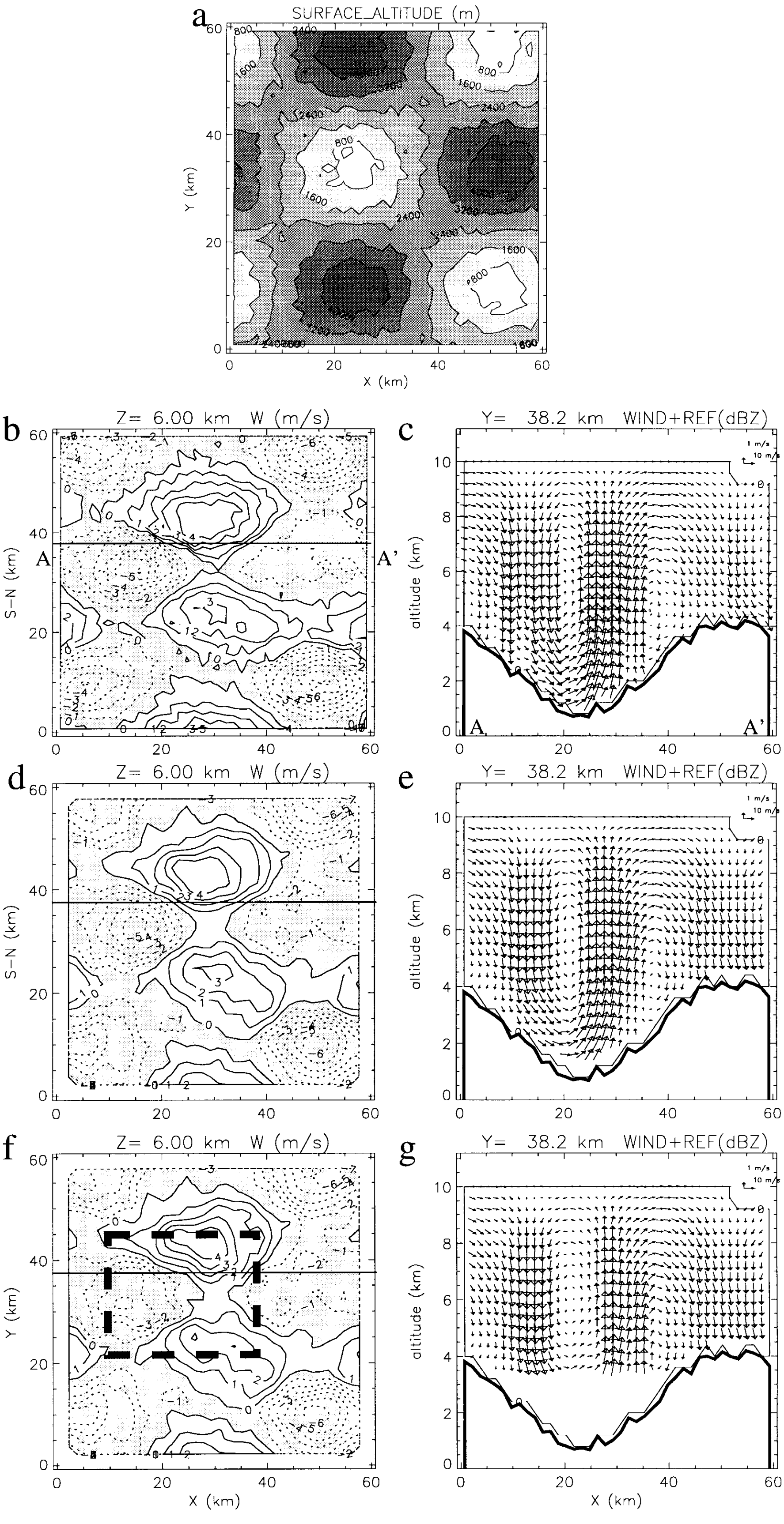

Fig. 2. Results from tests with anaytically simulated orography [contours in m in (a)] and wind fields: (b): horizontal cross-section of the simulated vertical velocity in ms^{-1} at 6 km altitude; (c) vertical cross-section along AA′ [at $\mathrm{Y} = 38.2$ km, as shown in (b)], scale is in the upper right; (d) and (e): as in (b) and (c), except for the wind field deduced with the method discussed in the text; (f) and (g): as in (d) and (e), except for missing input data below 3.2 km [dashed line contour at $11 < \mathrm{X}$ 38 km, $23 < \mathrm{Y} < 46$ km in (f)]

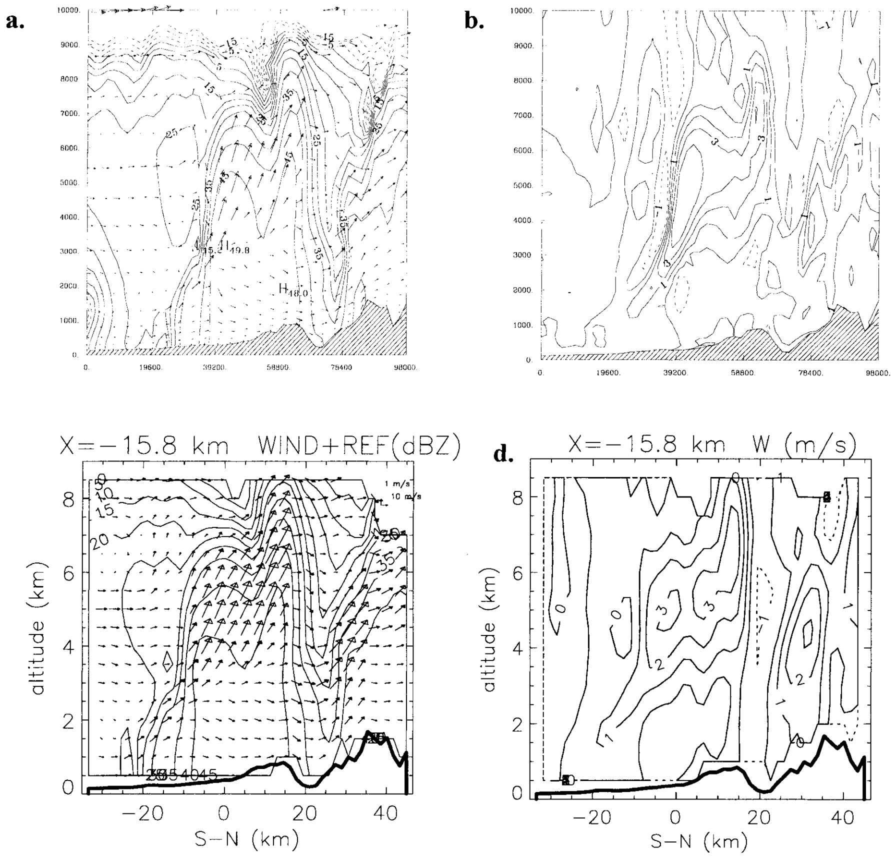

Fig. 3. North-south vertical section along 8.3° E through the three-dimensional wind field for the Brig flashflood on 22 September 1993 superimposed on the radar reflectivity (a and c) and corresponding vertical velocity (b and d). Data sources are a simulation by Cosma and Richard (1998) (upper panels: a and b), and the processing of simulated airborne Doppler radar observations (lower panels: c and d). The simulated radar data are from a pseudo-flight track roughly parallel to the section, but about 30 km to the west, with the scanning characteristics of ELDORA-ASTRAIA

deduced from comparisons between Fig. 2c, e and g.

Results from numerical model simulations of the heavy precipitation event on 22 September 1993 over northwestern Italy and southern Switzerland (the «Brig» case, Cosma and Richard 1998) have also been used to test the method (Fig. 3). A set of pseudo-Doppler data was obtained by using the scanning characteristics of ELDORA-ASTRAIA airborne Doppler radar for a simulated 60-km long northeastward leg at 6 km altitude above mean sea level (MSL). A gaussian white noise of 2 ms^{-1} rms value was added to the model-derived radial velocities to simulate radar error. As seen in Table 1, the rms values of horizontal wind and added correction are 14.97 and 1.52 ms^{-1}, respectively, those of horizontal divergence and added correction are 0.67 and 0.17×10^{-3} s^{-1}, respectively. The rms values of vertical velocity at echo top and of its horizontal gradient throughout the domain decrease from 2.62 to 0.23 ms^{-1}, and from 1.10 to 0.22×10^{-3} s^{-1}, respectively. Standard deviations between the retrieved and « actual » horizontal and vertical winds are 1.55 and 0.44 ms^{-1}, respectively. Comparisons between Fig. 3a and b show that the the pseudo Doppler-derived fields display similar, though slighlty smoother, characteristics.

6. Application to the Case of 12 March 1995 over Colorado

On 11–12 March 1995, a test flight was conducted with the NCAR Electra aircraft over northern Arizona and southern Colorado. The French-American ASTRAIA-ELDORA airborne Doppler radar was operated during this flight. From 0320 till 0400, the aircraft flew in an area of snow showers over the San Juan mountains characterized by high peaks up to about 4000 m MSL, as well as long and deep valleys. Although it concerns relatively weak precipitating clouds, this data set provides a unique opportunity to test the reliability of the above method for real. Here, we focus more particularly on a small area of 75 km×75 km centered on [38.3° N, 107.2° W] where the most active part of the precipitating system was observed. Below X and Y denote the eastward and northward horizontal axes, respectively.

Figure 4 shows the surface characteristics. The digital terrain map (Fig. 4a) reveals the presence of high peaks up to 4000 m altitude with deep valleys at $X=-10$ and $+10$ km in the southern part of the domain, a relatively flat zone at about 2400 m altitude at $-20<X<+35$ km and $5<Y<25$ km, and mountains up to 3200 m to the northern edge. The horizontal components of surface wind (Fig. 4b), extrapolated from the radar measurements aloft using the method described in Section 4, are fairly consistent with this orography. In particular, stronger winds apparently result from the canalization of the southeasterly flow by the valleys in the southern part, with some acceleration due to the downward slope, and by the pass near $X=+20$ km, $Y=+35$ km. The weaker and, in some places, swirling winds observed over the « plateau» at $5<Y<25$ km could result from wake effects downwind of the highest peaks to the south. The vertical component of surface wind (Fig. 4c) clearly reveals the importance of orography in the atmospheric circulation. Due to the prevailing southwesterly flow and the overall topography, downward motions (up to -2 ms^{-1}) are predominantly found in the southwestern half of the domain, except for some localized but strong updrafts south of the highest peaks, while slightly weaker (up to $+1$ ms^{-1}) upward motions occur on the southern flank of the mountains to the north. It must however be mentioned that the real surface flow may have been slightly different since, in addition to the uncertainties which certainly result from extrapolation, we made the very simple hypothesis of frictionless flow for the boundary layer circulation.

As seen in Table 1, the rms values of the horizontal wind and correction are 15.69 and 3.10 ms^{-1}, respectively; those of horizontal divergence are 1.57 and 0.66×10^{-3} s^{-1}. These corrections are slightly larger than those for the simulated

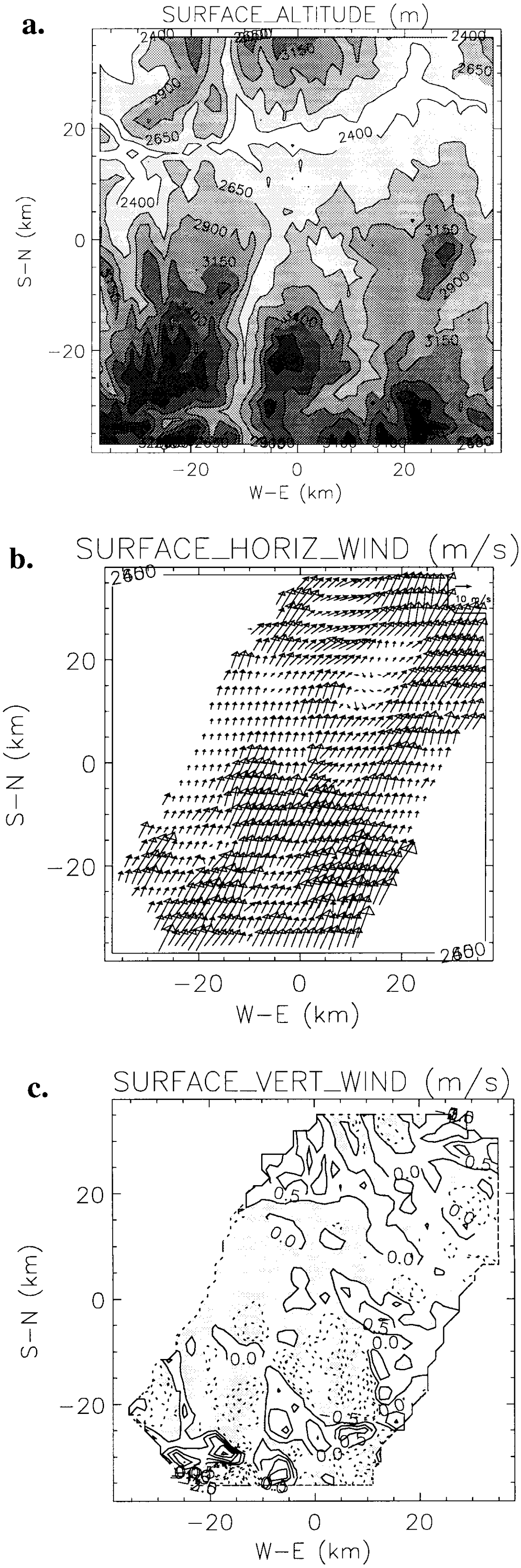

Fig. 4. (a) Terrain elevation map (contours every 250 m) derived from a digital terrain map for the considered domain of 75 km×75 km centered on 38.3° N, 107.2° W, (b) horizontal component of the surface wind (scale in the upper right), (c) vertical component of the surface wind (contours every 0.5 ms^{-1}, shaded zones denote downward motions)

Table 1. *Characteristics of the Analyzed Wind Fields: the Rows, from top to Bottom, are for the rms Values (Symbol <>) of Horizontal Wind and Added Correction, Horizontal Divergence and Added Correction, Vertical Velocity at the Top of the Domain before and after Correction has been Applied, Horizontal Gradient of Vertical Velocity Throughout the Domain before and after Correction has been Applied, Standard Deviations Between the Corrected Horizontal and Vertical Winds and the «actual» Values, respectively. Subscript «H» Indicates Horizontal Components*

	Analytical	Retrieved	Missing low-level data	«Brig» simulated ELDORA-ASTRAIA	12 March 1995
$\langle V_H \rangle (\mathrm{ms}^{-1}$	7.48	7.99	7.96	14.97	15.69
$\langle \Delta V_H \rangle (\mathrm{ms}^{-1})$	x	1.93	1.73	1.52	3.10
$\langle \mathrm{DIV_H} \rangle (10^{-3}\,\mathrm{s}^{-1})$	0.68	1.06	1.06	0.67	1.57
$\langle \Delta\mathrm{DIV_H} \rangle (10^{-3}\,\mathrm{s}^{-1})$	x	0.19	0.21	0.17	0.66
$\langle W_{\mathrm{top}} \rangle_{\mathrm{before}} (\mathrm{ms}^{-1})$	<0.01	3.25	3.76	2.62	4.00
$\langle W_{\mathrm{top}} \rangle_{\mathrm{after}} (\mathrm{ms}^{-1})$	x	0.10	0.10	0.23	0.36
$\langle \nabla_H W \rangle_{\mathrm{before}}\ (10^{-3}\,\mathrm{s}^{-1})$	0.53	2.04	2.36	1.10	1.42
$\langle \nabla_H W \rangle_{\mathrm{after}} (10^{-3}\,\mathrm{s}^{-1})$	x	0.44	0.43	0.22	0.37
$\sigma(V_H)(\mathrm{ms}^{-1})$	x	1.11	1.15	1.55	x
$\sigma(W)(\mathrm{ms}^{-1})$	x	0.45	0.52	0.44	x

data. Applying these corrections decreases the rms value of vertical velocity at echo top and its horizontal gradient throughout the domain from 4.00 to 0.36 ms^{-1}, and from 1.42 to $0.37 \times 10^{-3}\,\mathrm{s}^{-1}$, respectively. It is not possible to precisely deduce the uncertainty in the retrieved wind components, but comparisons with the results from simulated data indicate that it should be about 1–1.5 and 0.5 ms^{-1} for the horizontal and vertical wind, respectively.

The reflectivity field at 6.4 km altitude (Fig. 5a), the highest level where substantial radar echoes were observed, shows a cell of about 10 km × 10 km horizontally, with maximum reflectivity values >25 dBZ, centered at X = 0 km, Y = 22 km. Other maxima >20 dBZ are also observed near the southeastern limit of the scanning region, but it was not possible to retrieve the wind components from the Doppler data there. A comparison with Fig. 4c reveals that these reflectivity cells aloft are fairly well correlated with regions of strong upward slope winds at surface level. As seen in the vertical cross sections of the wind and reflectivity fields (Fig. 5c and d at Y = 20 km, e and f at X = 3.5 km), the largest reflectivity values are associated with predominantly upward motions where water vapour condenses into cloud droplets and rain drops or, more probably, into ice crystals and snow aggregates. Likewise, lower reflectivity values are found in regions of downward motions, where evaporation should occur.

The overall influence of orography on the wind and reflectivity fields clearly appears in Fig. 5e, with subsidence and decreasing reflectivity values above the downward slope at $-20<\mathrm{Y}<10$ km, upward motions and increasing reflectivity values above the upward slope at $15<\mathrm{Y}<30$ km. However, a small and shallow cell centered at $\mathrm{Y} = -10$ km is associated with downward or horizontal motions, which may seem incoherent. It is possible that small-scale orographic forcing induces a localized updraft, which is not resolved in the radar data analysis due to the relatively coarse horizontal grid spacing (1.5 km) used in this study. A similar conclusion on the importance of small-scale orographic effects is one of the major results obtained from pre-MAP modeling studies (Stein et al., 1998). This also shows the importance of having as precise radar observations as possible, so as to be able to retrieve coherent wind and reflectivity fields.

7. Conclusions

The aim of this study was to show that it is possible to use ground-based or airborne Doppler radar for quantitative observations of wind and

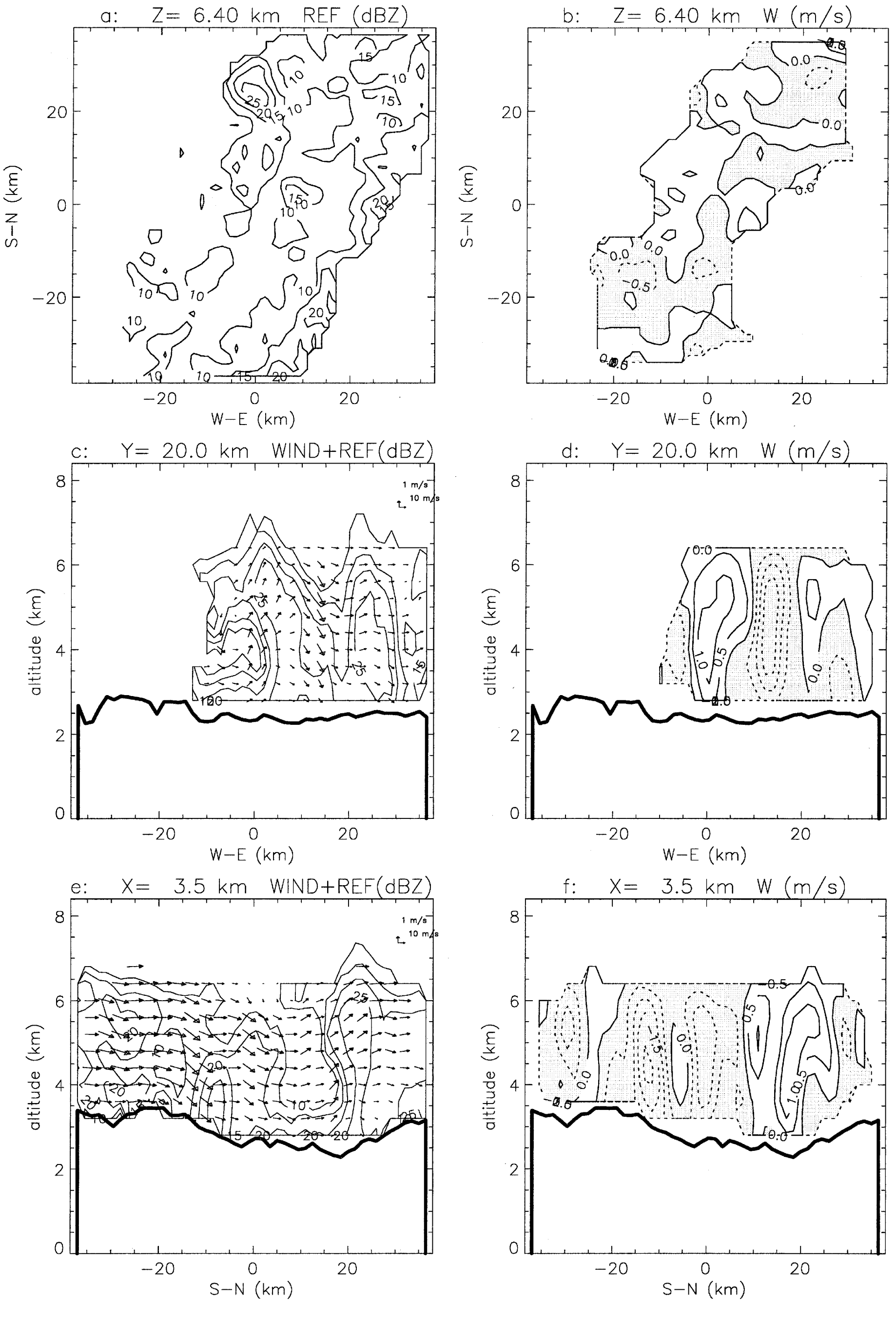

Fig. 5. (a) Reflectivity contours in dBZ at 6.4 km altitude for the same domain as in Fig. 3, (b) vertical motions at 6.4 km altitude (contours every 1 ms^{-1}, shaded zones denote downward motions); (c) wind (scale in the upper right) and reflectivity (contours every 4 dBZ) and (d) vertical velocity contours, for the zonal vertical cross section at Y = 20 km; (e) and (f) as in (c) and (d), except for the meridional vertical cross-section at X = 20 km. The thick line in (c), (d), (e) and (f) is the orography contour

precipitation fields over mountainous terrains, provided that the effects of orography in radar data and in the airflow are explicitely taken into account.

Firstly, we have shown that the surface echoes can be unambiguously identified in the radar data and separated from the meteorological signal, and that a comparison with a digital terrain map helps to deduce the navigational corrections which have to be taken into account for reliable information to be retrieved from Doppler data. Secondly, we have shown that the rôle of orography through the induced slope winds at surface level can be included in the variational analysis aimed at deriving balanced three-dimensional wind fields from the integration of the air mass continuity equation. Application of these new techniques to analytical wind fields and orographies, to pseudo-Doppler observations using numerical model outputs from the simulation of a heavy precipitation event (the «Brig case» of 22 September 1993), and to actual data collected with the ELDORA-ASTRAIA airborne Doppler radar within weak snow showers over the Rocky Mountains, have shown the reliability of this approach. Nevertheless, it should be mentioned that sampling of a given atmospheric volume with ground-based and airborne Doppler radar takes some time and that further uncertainties could result from non-simultaneous measurements, especially for rapidly developing systems.

Of course, more studies are needed to more completely validate the proposed method. We are however confident that, in this manner, it will be possible to obtain reliable information on the structure and evolution of the precipitation and kinematic fields associated with orographically induced or modified precipitating systems, to be observed with airborne (ELDORA-ASTRAIA onboard the NCAR Electra, Tail Doppler radar onboard the National Oceanic and Atmospheric Administration's P3 aircraft) and ground-based (Swiss Meteorological Institute operational Doppler at Monte-Lema, US NCAR Doppler and polarimetric S-Pol, French Doppler Ronsard) radars during the MAP Special Observing Period (7 September–15 November 1999).

Appendix
The Derivatives of x_{RAD}, y_{RAD}, z_{RAD}, V_{RAD} and V_{INSITU}

Following Lee et al. (1994) and Testud et al. (1995), the natural variables for airborne Doppler radar observations are:

(i) the radar-relative angles indicating the direction toward which the antenna is pointing: « tilt » τ [angle from the plane perpendicular to the spin axis of the radar beam, positive (negative) when the antenna points fore (aft)] and «rotation» θ [spin angle defined through a projection onto a plane perpendicular to the fuselage, 0° is along the tailplane, +90° (+270°) along the right (left) wing];

(ii) the aircraft-relative angles indicating the aircraft (or radar) attitude: « roll » R (angle between the wings and the horizontal plane during a rotation along the aircraft longitudinal axis, positive when the right wing is down), « heading » H (angle measured clockwise from north to the projection of the aircraft longitudinal axis to the horizontal plane) and «pitch» P (angle that the aircraft longitudinal axis makes with the horizontal plane).

These angles can be combined to deduce the « earth-relative azimuth » α (relative to east, increasing counter-clockwise) and « elevation » β (nadir is −90°, horizontal is 0°, zenith is +90°). Each ray is then defined by three normalized coefficients $(C_X^2 + C_Y^2 + C_Z^2 = 1)$:

$$\begin{aligned}
C_X &= \cos\alpha\cos\beta \\
&= [-\cos(\tau)\cos(\theta+R)\sin(P) + \sin(\tau)\cos(P)]\sin(H) \\
&\quad + \cos(\tau)\sin(\theta+R)\cos(H) \\
C_Y &= \sin\alpha\cos\beta \\
&= [-\cos(\tau)\cos(\theta+R)\sin(P) + \sin(\tau)\cos(P)]\cos(H) \\
&\quad - \cos(\tau)\sin(\theta+R)\sin(H) \\
C_Z &= \sin\beta = \cos(\tau)\cos(\theta+R)\cos(P) + \sin(\tau)\sin(P)
\end{aligned}$$

The cartesian coordinates x_{RAD}, y_{RAD}, z_{RAD} (x, y, z are positive eastward, northward and upward, respectively) of a point measured at distance d from the radar with the above angles are then:

$$\begin{aligned}
x_{\mathrm{RAD}} &= x_{\mathrm{AC}} + d \times C_X \\
y_{\mathrm{RAD}} &= y_{\mathrm{AC}} + d \times C_Y \\
z_{\mathrm{RAD}} &= z_{\mathrm{AC}} + d \times C_Z
\end{aligned}$$

where x_{AC}, y_{AC}, z_{AC} are the aircraft cartesian coordinates with respect to given latitude, longitude and altitude. The derivatives of these quantities with respect to angles (R, P, H), distances (x, y, z) and ranging (d; d_f and d_a being relative to the fore and aft radar, respectively) that appear in (1) are then:

$$\begin{aligned}
\frac{\partial x_{\mathrm{RAD}}}{\partial R} &= d \times \frac{\partial C_X}{\partial R} = d \times \cos(\tau)[\sin(\theta+R)(\sin(P)\sin(H) \\
&\quad + \cos(\theta+R)\cos(H)]
\end{aligned}$$

$$\begin{aligned}
\frac{\partial x_{\mathrm{RAD}}}{\partial P} &= d \times \frac{\partial C_X}{\partial P} = d \times [-\cos(\tau)\cos(\theta+R)\cos(P)\sin(H) \\
&\quad - \sin(\tau)\sin(P)\sin(H)]
\end{aligned}$$

$$\begin{aligned}
\frac{\partial x_{\mathrm{RAD}}}{\partial H} &= d \times \frac{\partial C_X}{\partial H} = d \times \{\sin(\tau)\cos(P)\cos(H) \\
&\quad - \cos(\tau)[\cos(\theta+R)\sin(P)\cos(H) \\
&\quad + \sin(\theta+R)\sin(H)]\}.
\end{aligned}$$

$$\frac{\partial x_{\mathrm{RAD}}}{\partial x} = 1 \quad \frac{\partial x_{\mathrm{RAD}}}{\partial y} = 0 \quad \frac{\partial x_{\mathrm{RAD}}}{\partial z} = 0 \quad \frac{\partial_{x_{\mathrm{RAD}}}}{\partial d} = C_X$$

$$\begin{aligned}
\frac{\partial y_{\mathrm{RAD}}}{\partial R} &= d \times \frac{\partial C_Y}{\partial R} = d \times \cos(\tau)[\sin(\theta+R)\sin(P)\cos(H) \\
&\quad - \cos(\theta+R)\sin(H)]
\end{aligned}$$

$$\begin{aligned}
\frac{\partial y_{\mathrm{RAD}}}{\partial P} &= d \times \frac{\partial C_Y}{\partial P} = d \times [-\cos(\tau)\cos(\theta+R)\cos(P)\cos(H) \\
&\quad - \sin(\tau)\sin(P)\cos(H)]
\end{aligned}$$

$$\begin{aligned}
\frac{\partial y_{\mathrm{RAD}}}{\partial H} &= d \times \frac{\partial C_Y}{\partial H} = d \times \{-\sin(\tau)\cos(P)\sin(H) \\
&\quad + \cos(\tau)[\cos(\theta+R)\sin(P)\sin(H) \\
&\quad - \sin(\theta+R)\cos(H)]\}
\end{aligned}$$

$$\frac{\partial y_{\mathrm{RAD}}}{\partial x}=0 \quad \frac{\partial y_{\mathrm{RAD}}}{\partial y}=1 \quad \frac{\partial y_{\mathrm{RAD}}}{\partial z}=0 \quad \frac{\partial y_{\mathrm{RAD}}}{\partial d}=C_Y$$

$$\frac{\partial z_{\mathrm{RAD}}}{\partial R}=d\times\frac{\partial C_Z}{\partial R}=d\times[-\cos(\tau)\sin(\theta+R)\cos(P)]$$

$$\frac{\partial z_{\mathrm{RAD}}}{\partial P}=d\times\frac{\partial C_Z}{\partial P}=d\times[-\cos(\tau)\cos(\theta+R)\sin(P) + \sin(\tau)\cos(P)]$$

$$\frac{\partial z_{\mathrm{RAD}}}{\partial H}=0$$

$$\frac{\partial z_{RAD}}{\partial x}=0\,\frac{\partial z_{\mathrm{RAD}}}{\partial y}=0\,\frac{\partial z_{\mathrm{RAD}}}{\partial z}=1\,\frac{\partial z_{\mathrm{RAD}}}{\partial d}=C_Z$$

The earth-relative Doppler velocity V_{RAD} [referred to as V_{SURF} in (2) or V_{NEAR} in (3)] is also influenced by the navigation errors, through an inadequate correction of the measuerd aircraft-relative Doppler velocity V_{MEAS} for the projection V_{AC} of the aircraft speed (cartesian components u_{AC}, v_{AC}, w_{AC} onto the direction of the radar beam. We have:

$$V_{\mathrm{RAD}}=V_{\mathrm{MEAS}}+V_{\mathrm{AC}}$$

$$V_{\mathrm{AC}}=C_X\times u_{\mathrm{AC}}+C_Y\times v_{\mathrm{AC}}+C_Z\times w_{\mathrm{AC}}$$

then

$$\frac{\partial V_{\mathrm{RAD}}}{\partial R}=\frac{\partial V_{\mathrm{AC}}}{\partial R}=u_{\mathrm{AC}}\frac{\partial C_X}{\partial R}+v_{\mathrm{AC}}\frac{\partial C_Y}{\partial R}+w_{\mathrm{AC}}\frac{\partial C_Z}{\partial R}$$

$$\frac{\partial V_{\mathrm{RAD}}}{\partial P}=\frac{\partial V_{\mathrm{AC}}}{\partial P}=u_{\mathrm{AC}}\frac{\partial C_X}{\partial P}+v_{\mathrm{AC}}\frac{\partial C_Y}{\partial P}+w_{\mathrm{AC}}\frac{\partial C_Z}{\partial P}$$

$$\frac{\partial V_{\mathrm{RAD}}}{\partial H}=\frac{\partial V_{\mathrm{AC}}}{\partial H}=u_{\mathrm{AC}}\frac{\partial C_X}{\partial H}+v_{\mathrm{AC}}\frac{\partial C_Y}{\partial H}$$

$$\frac{\partial V_{\mathrm{RAD}}}{\partial V}=\frac{\partial V_{\mathrm{AC}}}{\partial V}=C_X\frac{\partial u_{\mathrm{AC}}}{\partial V}+C_Y\frac{\partial v_{\mathrm{AC}}}{\partial V}=C_X\sin(H+D) + C_Y\cos(H+D)$$

where D is the «drift» angle, between the heading and the track angles. The track is the angle measured clockwise from the north to the aircraft ground trajectory, a positive drift being defined as the track more clockwise than the heading. The expressions for the derivatives of $\mathrm{C_X}$, $\mathrm{C_Y}$ and $\mathrm{C_Z}$ are given above. Likewise, errors in the projection of the flight-level wind components is supposed to result only from errors in pitch, drift and heading angles, as:

$$V_{\mathrm{INSITU}}=C_X\times u_{\mathrm{INSITU}}+C_Y\times v_{\mathrm{INSITU}}+C_Z\times w_{\mathrm{INSITU}}$$

then:

$$\frac{\partial V_{\mathrm{INSITU}}}{\partial R}=u_{\mathrm{INSITU}}\frac{\partial C_X}{\partial R}+v_{\mathrm{INSITU}}\frac{\partial C_Y}{\partial R}+w_{\mathrm{INSITU}}\frac{\partial C_Z}{\partial R}$$

$$\frac{\partial V_{\mathrm{INSITU}}}{\partial P}=u_{\mathrm{INSITU}}\frac{\partial C_X}{\partial P}+v_{\mathrm{INSITU}}\frac{\partial C_Y}{\partial P}+w_{\mathrm{INSITU}}\frac{\partial C_Z}{\partial P}$$

$$\frac{\partial V_{\mathrm{INSITU}}}{\partial H}=u_{\mathrm{INSITU}}\frac{\partial C_X}{\partial H}+v_{\mathrm{INSITU}}\frac{\partial C_Y}{\partial H}$$

Acknowledgments

We are indebted to Dr. Evelyne Richard and Ms. Stéphanie Cosma, from Laboratoire d'Aérologie, who kindly provided numerical model outputs from the Brig case to simulate radar observations. ASTRAIA-ELDORA radar is the result of the joint efforts of National Center for Atmospheric Reserach / University Corporation for Atmospheric Research (Boulder, Co., USA) and Institut National des Sciences de l'Univers (INSU) / Centre National de la Recherche Scientifique (Paris, France). This study was sponsored by European Commission / Environment and Climate Programme under contract ENV4-CT96-0332 (efficiently coordinated by Hans Volkert, DLR Oberpfaffenhofen, Germany) and, marginally, by INSU/PATOM (Programme Atmosphère et Océan à Moyenne Echelle) grants 96/01, 97/09, 98/03. Constructive comments made by the two anonymous reviewers helped to improve this paper.

References

Bijlsma, S. J., Hafkenscheid, M., Lynch, P., 1986: Computation of the streamfunction and velocity potential and reconstruction of the wind field. *Mon. Wea. Rev.,* **114**, 1547–1551.

Binder, P., Bougeault, P., Buzzi, A., Davies, H. C., Heimann, D., Hoinka, K. P., Kuettner, J. P., Majewski, D., Mayr, G., Schär, C., Smith, R. B., Steinacker, R., Volkert H., Whiteman, C. D., 1995: Mesoscale Alpine Programme: Design proposal. Available upon request at MAP Data Centre, ETH Zürich, Switzerland, 65 pp.

Bond, N. A., Mass, C. F., Smull, B. F., Houze, R. A., Yang, M. -J., Colle, B. A., Braun, S. A., Shapiro, M. A., Colman, B. R., Neiman, R. J., Overland, J. E., Neff, W. D., Doyle, J. D., 1997: The Coastal Observation and Simulation with Topography (COAST) Experiment. *Bull. Amer. Meteor. Soc.,* **78**, 1941–1955.

Braun, S. A., Houze, R. A., Jr., Smull, B. F., 1997: Airborne dual-Doppler observations of an intense frontal system approaching the Pacific Northwest coast. *Mon. Wea. Rev.,* **125**, 3131–3156.

Chong, M., Testud, J., 1983: Three-dimensional wind field analysis from dual-Doppler radar data. Part III: The boundary condition: An optimum determination based on a variational concept. *J. Climate Appl. Meteor.,* **22**, 1227–1241.

Cosma, S., Richard, E., 1998: Simulations numériques de l'épisode de précipitations intenses de Brig. *Atelier de Modélisation de l'Atmosphère,* Météo-France, 8–9 December 1998, Toulouse, France, 9–12.

Cotton, W. R., George, R. L., Wetzel, P. J., McAnelly, R. L., 1983: A long-lived mesoscale convective complex. Part I: The mountain-generated component. *Mon. Wea. Rev.,* **111**, 1893–1918.

Cressman, G. P., 1959: An operational objective analysis system. *Mon. Wea. Rev.,* **87**, 367–374.

Delrieu, G., Creutin J. -D., Andrieu, H., 1995: Simulation of radar mountain returns using a digitized terrain model. *J. Atmos. Oceanic Technol.,* **12**, 1038–1049.

Hestenes, M. R., Stieffel, E., 1952: Methods of conjugate-gradients for solving linear systems. *J. Res. Natl. Bur. Stand.,* **48**, 409–436.

Hildebrand, P. H., Walther, C. A., Frush, C. L., Testud, J., Baudin, F., 1994: The ELDORA/ASTRAIA airborne Doppler weather radar: Goals, design, and first field tests. *Proc. IEEE.,* **82**, 1873–1890.

Lee, W.-C., Dodge, P., Marks, Jr., F. D., Hildebrand, P. H., 1995: Mapping of airborne Doppler radar data. *J. Atmos. Oceanic Technol.,* **11**, 572–578.

Matejka, T., Bartels, D. L., 1998: The accuracy of air velocities from Doppler radar data. *Mon. Wea. Rev.,* **126**, 92–117.

Ray, P. S., Ziegler, C. L., Bumgarner, W., Serafin, R. J., 1980: Single and multiple Doppler radar observations of tornadic storms. *Mon. Wea. Rev.,* **108**, 1607–1625

Roux, F., Sun, J., 1990: Single-Doppler observations of a West-African squall line on 27–28 May 1981 during COPT 81: Kinematics, thermodynamics and water budget. *Mon. Wea. Rev.,* **118**, 1826–1854.

Roux, F., Marécal, V,. Hauser, D., 1993: The narrow cold-frontal rainband observed on 12–13 January 1988 during the MFDP/FRONTS 87 experiment. Part I: Kinematics and thermodynamics. *J. Atmos. Sci.,* **50**, 951–974.

Roux, F., Viltard, N., 1995: Structure and evolution of Hurricane Claudette on 7 September 1991 from airborne Doppler radar observations. Part I: Kinematics. *Mon. Wea. Rev.,* **123**, 2611–2639.

Stein, J., Richard, E., Lafore, J. P., Pinty, J. P., Asencio, N., Cosma, S., 1999: Meso-NH simulations with grid-nesting and ice-phase parameterization. *Meteorol. Atmos. Phys.* (special issue on HERA) (to appear).

Testud, J., Hildebrand, P. H., Lee, W.-C., 1995: A procedure to correct airborne Doppler radar data for navigation errors using the echo returned from the Earth's surface. *J. Atmos. Oceanic Technol.,* **12**, 800–820.

Authors' addresses: Jean-François Georgis, Frank Roux, Laboratoire d'Aérologie (CNRS-UPS), 14 av. Edouard Belin, F-31400 Toulouse, France; Laboratoire d'Aérologie, Peter H. Hildebrand, National Center for Atmospheric Research, Boulder, CO, USA.